AGU PUBLICATIONS

Geophysical Research Letters

Supporting Information for

Sources and pathways of iron into the Pacific Equatorial Undercurrent

Xuerong Qin [1], Laurie Menviel [1], Alex Sen Gupta [1], Erik van Sebille [1,2]

[1] Climate Change Research Centre & ARC Centre of Excellence on Climate System Science,

The University of New South Wales, Sydney, Australia.

[2] Grantham Institute & Department of Physics, Imperial College London, United Kingdom.

Contents of this file

Text S1 to S9
Figures S1 to S7
Table S1 to S2

S1. Schematic of the circulation in the Western Pacific

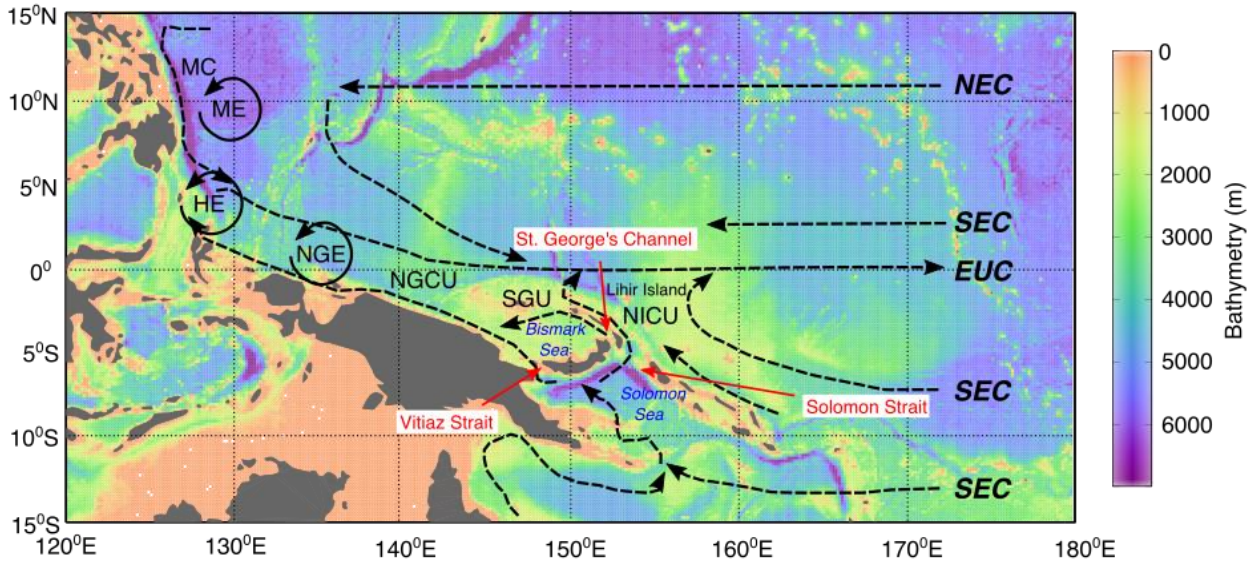

Figure S1. ***Schematic map of the western tropical Pacific Ocean circulation.*** *The currents are the North Equatorial Current (NEC), South Equatorial Current (SEC), St Georges Undercurrent (SGU), Mindanao Current (MC), New Guinea Coastal Undercurrent (NGCU), New Ireland Coastal Undercurrent (NICU), and Equatorial Undercurrent (EUC). The Mindanao Eddy (ME), the Halmahera Eddy (HE), and the New Guinea Eddy (NGE) are also shown. Modified from Grenier et al. [2011].*

S2. OFAM3 validation

As detailed in *Qin et al.* [2015], the characteristics of the EUC are simulated relatively well in OFAM3. In particular, the variability of the EUC is reproduced successfully but some biases exist in the mean EUC transport. Here we focus on evaluating the characteristics of the NGCU and particularly interannual variability in NGCU transport and zonally averaged velocities for El Niño and neutral years at 142^0E (Figure S2). The mean NGCU transport in OFAM3 is consistent with the observed moored ADCP transport at 2.5^0S 142^0E (*Ueki et al.* [2003], Figure S2a) at the 95 % confidence level, with very similar variability (standard deviations of 4.8 vs. 5 Sv for simulated and observed current transports, respectively).

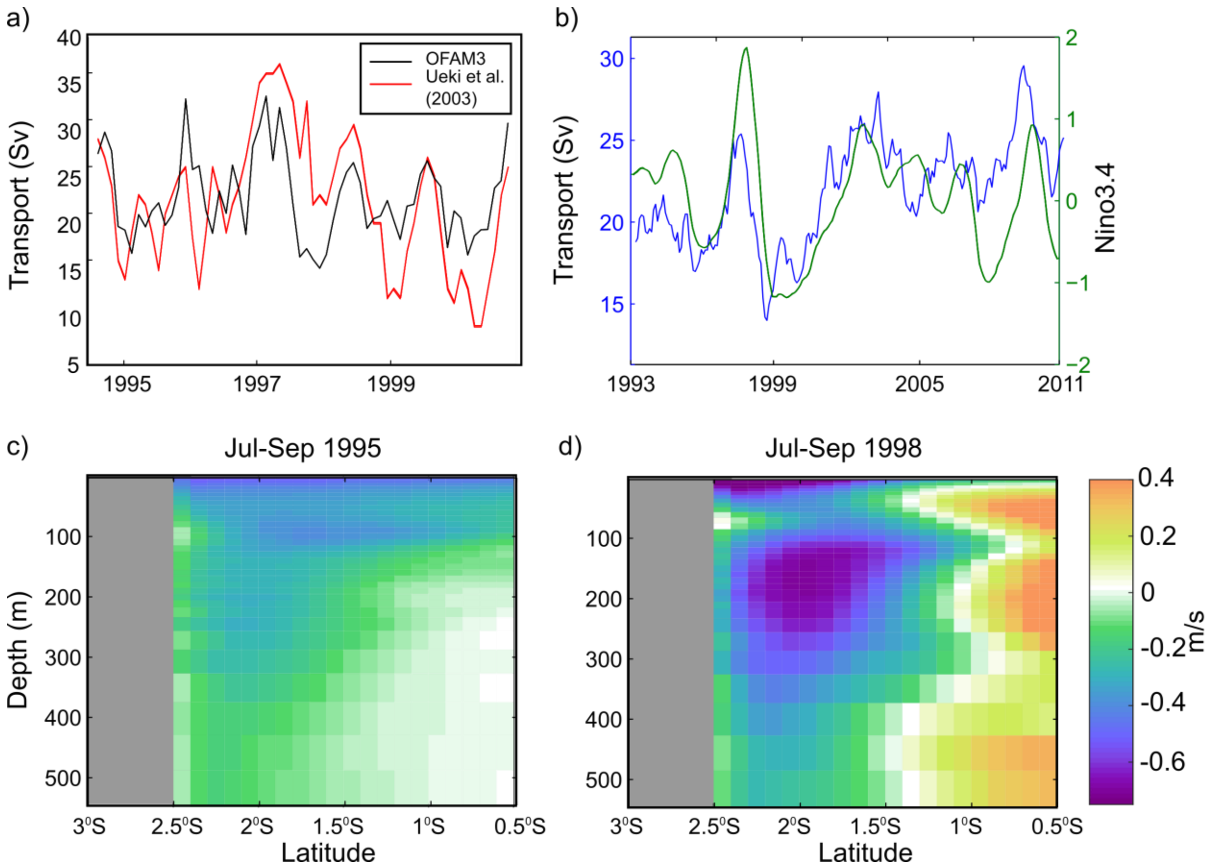

Figure S2. ***NGCU variability.*** *Time series of OFAM3 NGCU transport at the meridional section at 3°S-0.5°S, 142°E compared with a) Ueki et al. [2003] (red) as monthly means (black) and b) OFAM3 Nino3.4 index (green) as 3-day series smoothed with a 6 month running average (blue). The transport and Nino3.4 index in b) are smoothed with a 6 month running average. The time averaged zonal velocity of the NGCU at 142°E during c) July-September 1995 (neutral year) and d) July-September 1998 (El Niño year).*

The simulated NGCU transport is anti-correlated (r= –0.47) with the model Nino3.4 index (Figure S2b), consistent with previous studies, such that NGCU transport is greatest during El Niño events and lowest during La Niña events. The zonal velocity in the core of the NGCU intensifies during El Niño years compared to neutral years (Figures S2c-d), in agreement with observations [*Ryan et al.*, 2006; *Ueki et al.*, 2003]. In addition, the core of the NGCU in OFAM3 is at ~200 m with a mean speed of 0.4 ms^{-1} which is in good agreement with observations [*Johnson et al.*, 2002; *Ueki et al.*, 2003]. The maximum speed of ~0.7 ms^{-1} is only marginally lower than the observed 0.8 ms^{-1} described in *Mackey et al.* [2002].

As for the NICU, the net Eulerian transport in OFAM3 at the section 5.1^0S, 152.1^0E-155.4^0E in the upper 300 m is 6 Sv with an annual range of 4.4-8.8 Sv. These values are at the high end but still comparable to the observations of 4-5 Sv [*Butt and Lindstrom*, 1994; *Cravatte et al.*, 2011]. As such, the NGCU and NICU are reproduced with considerable fidelity in OFAM3.

Next, we consider how well OFAM3 simulates equatorial productivity, as this affects iron remineralisations and phytoplankton uptake of iron (see Equations A1-A10). The fidelity of Chlorophyll-a (Chl-a) in OFAM3 is examined by comparison with observed Chl-a from SeaWIFS (http://oceandata.sci.gsfc.nasa.gov/SeaWiFS/). The tropical Pacific SeaWiFS mean Chl-a field (Figure S3b) is highest along the equator, extending from the coast of South America to about 150^0E – 160^0E. These features are evident in the model estimates but the Chl-a values are overestimated off the Equator in the Central Pacific, while being underestimated in the Eastern Equatorial Pacific.

Observed Chl-a variance is high along the equator associated with variability in wind driven upwelling (Figure S3d). There are also two zonal bands of high Chl-a variability in the central and eastern tropical Pacific, at about 5°N and 10°N that are associated with the North Equatorial Current and the North Equatorial Counter Current respectively [*Oke et al.*, 2012]. Compared to SeaWiFS, OFAM3 variability (Figure S3c) is relatively lower along the equator, while variability off the equator is much higher. As remineralisation of organic matter at depth increases the iron concentration, an underestimated export production in the EEP at 110°W could lead to less sinking of organic matter and an underestimation of the simulated iron content in the EUC. However, as mentioned in previous studies [*Gorgues et al.*, 2010], and diagnosed in our iron budget calculations the contribution of biological activity to changes in EUC iron is more than an order of magnitude smaller than due to scavenging.

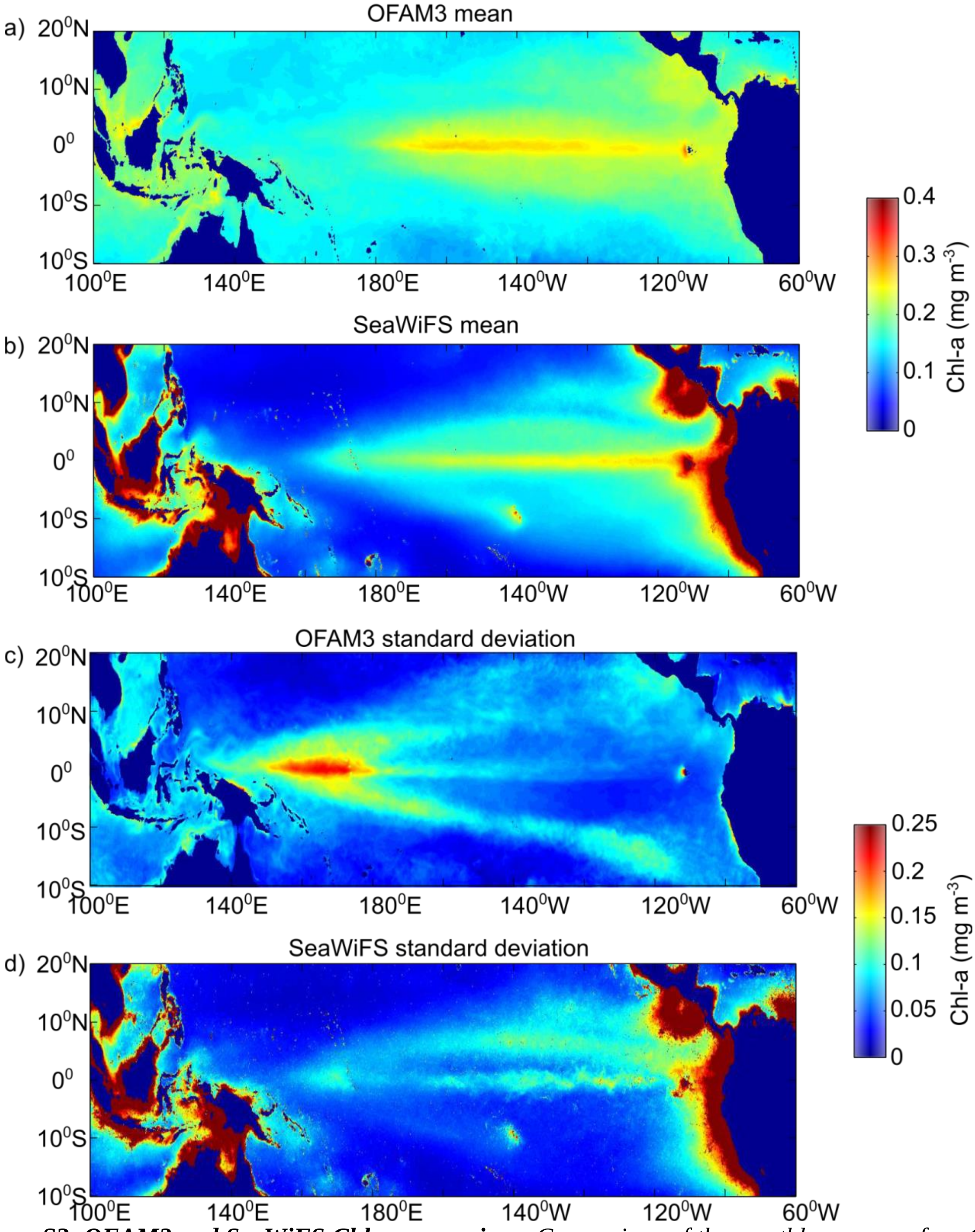

Figure S3. ***OFAM3 and SeaWiFS Chl-a comparison.*** *Comparison of the monthly mean surface Chl-a from a) OFAM3 and b) SeaWIFS and Chl-a standard deviation from c) OFAM3 and d) SeaWIFS.*

S3. Model Description

In Lagrangian form, the equation for the evolution of iron along a Lagrangian particle trajectory is given by:

$$\frac{D\boldsymbol{Fe}}{Dt} = Fe_{src} + Fe_{reg} - Fe_{phy} - Fe_{scav} \qquad \text{(A1)}$$

in which iron change $D\boldsymbol{Fe}/Dt$ in nM day^{-1}.

The biological terms, remineralization (Fe_{reg}) and uptake by phytoplankton (Fe_{phy}), are calculated according to the parameterisations used in Whole Ocean Model with Biogeochemistry and Trophic-dynamics (WOMBAT) biogeochemical model which is coupled to OFAM3 [*Oke et al.*, 2012].

$$Fe_{reg} = 0.02 \times (\mu_D Det + \gamma_2 Z + \mu_P P) \qquad \text{(A1)}$$

$$Fe_{phy} = 0.02 \times \bar{J}(z, t, T, N, \boldsymbol{Fe})P) \qquad \text{(A2)}$$

Fe_{reg} is a combination of organic matter remineralised from detritus (*Det*), zooplankton (*Z*) excretion, and phytoplankton (*P*) mortality. Fe_{phy} is the uptake of iron for phytoplankton growth, which is a function of temperature (*T*), light (*I*) and nutrient concentration (nitrate (*N)* and ***Fe***). A factor of 0.02 in Equations A1 and A2 is used to relate changes in iron to nitrate using a Redfield molar ratio for Fe:N of 2.0×10^{-5}:1. *P, Z and Det* are expressed in units of mmol N m^{-3} and ***Fe*** is in μmol.m^{-3} (nM).

$\boldsymbol{Fe}$ is the only prognostic variable in the iron model and is indicated in bold while all other variables (*T*, *N*, *P*, *Z*, *Det*) are taken from OFAM3. In OFAM3, changes in *P, Z* and *D* are calculated as described in *Oke et al.* [2012]:

$$\frac{DP}{Dt} = \bar{J}(z,t,T,N,\boldsymbol{Fe})P - G(P,Z) - \mu_P P \quad \text{(A3)}$$

$$\bar{J}(z,t,T,N,\boldsymbol{Fe}) = J_{max}(T) \times min\left[\frac{J(z,t,T)}{J_{max}(T)}, \frac{N}{N+k_N}, \frac{\boldsymbol{Fe}}{\boldsymbol{Fe}+k_{Fe}}\right] \quad \text{(A4)}$$

$$J(z,t,T) = J_{max}(T)\left(1 - e^{-\alpha I(z,t)/J_{max}(T)}\right) \quad \text{(A5)}$$

$$I(z,t) = PAR \times I(0,t) \times Frac \quad \text{(A6)}$$

$$J_{max}(T) = ab^{cT} \quad \text{(A7)}$$

$$\frac{DZ}{Dt} = \gamma_1 G(P,Z) - \gamma_2 Z - \mu_Z Z^2 \quad \text{(A8)}$$

$$G(P,Z) = \frac{g\varepsilon P^2}{g + \varepsilon P^2} Z \quad \text{(A9)}$$

$$\frac{DDet}{Dt} = (1-\gamma_1)G(P,Z) + \mu_Z Z^2 - \mu_D Det - w_D \frac{dDet}{dz} \quad \text{(A10)}$$

DP/Dt, DZ/Dt and $DDet/Dt$ are calculated as a local effect rather than evolved along the trajectory as with *Fe* in Equation 1. That is, the *P*, *Z* and *Det* values to be used in Equations A1 and A2 are updated at each point along the Lagrangian trajectory from solving Equations A3, A9 and A10 using the previous $\boldsymbol{Fe}$ calculated along the Lagrangian trajectory but using the local Eulerian WOMBAT *P*, *Z* and *Det* values from the previous time step. In this way, the concentration of iron along the trajectory still has some impact on the biological effect. The implications of having a local biological effect not evolved along the trajectory are discussed in Text S7.

Changes in phytoplankton (DP/Dt) depends on the growth term $\bar{J}(z,t,T,N,\boldsymbol{Fe})P$, grazing by zooplankton $G(P,Z)$ and mortality ($\mu_P P$). $\bar{J}(z,t,T,N,\boldsymbol{Fe})$ governs the phytoplankton growth rate and is a function of temperature (*T*), light (*I*) and nutrient concentration (*N* and $\boldsymbol{Fe}$). The growth rate $\bar{J}$ is given by Equations A4-A7 where J_{max} is the maximum phytoplankton growth at a given T, assuming no light or nutrient limitation; $J(z,t,T)$ is the impact of light on growth rate. Equation A8 describes the zooplankton, represented as the balance between growth due to phytoplankton grazing $G(P,Z)$ and losses due to zooplankton excretions ($\gamma_2 Z$) and mortality ($\mu_Z Z^2$). Grazing of phytoplankton ($G(P,Z)$, Equation A9) depends on the efficiency of zooplankton grazing on phytoplankton. Equation A10 describes the detritus changes and includes input from zooplankton grazing and mortality, as well as terms for detrital decomposition ($\mu_D Det$) and sinking ($w_D \times dDet/dz$). See Table S1 for parameter values and descriptions.

Parameter	**Units**	**Value**	**Description**
		Phytoplankton parameters	
α	day^{-1}/(W m^{-2})	0.025	Initial slope of P-I curve
PAR	-	0.34	Photosynthetically active radiation
a	day^{-1}	0.6	Growth rate at 0^{o}C
b	-	1.066	Temperature sensitivity of growth
c	C^{-1}	1.0	Growth rate reference for light limitation
k_N	mmol N m^{-3}	1.0	Half-saturation constant for nitrate
k_{Fe}	day^{-1}	1.0	Half-saturation constant for iron
μ_P	day^{-1}	0.01 b^{cT}	Mortality of phytoplankton
		Zooplankton parameters	
γ_1	-	0.85	Grazing efficiency
g	day^{-1}	2.1	Maximum grazing rate
ε	(mmol N m^{-2})$^{-1}$ day^{-1}	1.1	Prey capture rate
μ_Z	(mmol N m^{-2})$^{-1}$ day^{-1}	0.06	Quadratic mortality
γ_2	day^{-1}	0.01 b^{cT}	Excretion rate
		Detritus parameters	
μ_D	day^{-1}	0.02 b^{cT}	Remineralisation rate (<180 m)
μ_D	day^{-1}	0.01 b^{cT}	Remineralisation rate (180 m)
w_D	m day^{-1}	10	Sinking velocity

Table S1. *Biological parameters of the iron model and their values taken from Oke et al. [2012].*

S4. Lagrangian iron model validation

We performed some initial experiments to test the efficacy of the Lagrangian iron model (main text: Equation 1) against simulated iron fields in OFAM3 (i.e. not using any observational constraints). The Lagrangian particle iron concentrations at the source sections,

Fe_{src}, were derived from the corresponding simulated OFAM3 iron values. The iron concentration of each particle was then calculated along its trajectory using Equation 1. The Lagrangian iron concentration calculated was then compared to the local Eulerian OFAM3 iron values once the particles reach 170°W.

The correlation between Lagrangian model and OFAM3 6-day iron concentration time series averaged spatially over all particles that reach the EUC core (as defined when particles are initialised) at 170°W is high (r = 0.97) and the time series means were not statistically different (Figure S4a). The spatial distributions on meridional sections were also similar (Figure S4b,c) although the concentration for the Lagrangian model is slightly higher at the core by 0.05 nM compared to OFAM3. The good agreement between the Lagrangian field and OFAM3 indicates that the Lagrangian iron model is largely performing as required. The comparison also demonstrates that vertical diffusion and iron deposition from atmospheric dust, which are not accounted for in the Lagrangian model, must be relatively small terms compared to the biological activity and scavenging terms. As such, neglecting vertical diffusion and iron deposition from atmospheric dust should not significantly impact the results.

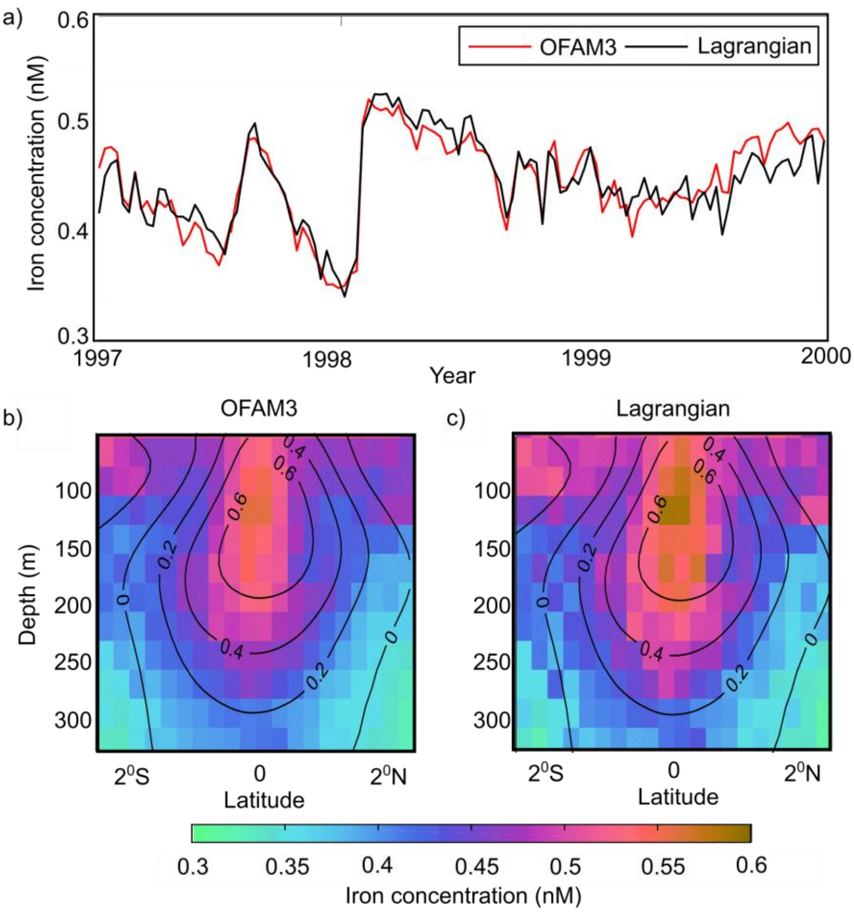

Figure S4. ***Lagrangian model validation against OFAM3.*** *A) Comparison of iron concentration between 1997 and 2000 at the EUC section 170^0W between the Lagrangian model iron (black) and OFAM3 (red) with a 6-day times series. A meridional slice of the time-averaged iron (1997 – 2000) at 170^0W in b) OFAM3 and c) Lagrangian model overlaid with OFAM3 zonal velocities contours (cm s^{-1}).*

S5. Optimizing scavenging

The scavenging parameters k_{Fe}^{org} and k_{Fe}^{inorg} in Equation 2 are adjusted to minimize the difference between Lagrangian iron estimates and the observations along the EUC through a systematic testing of different parameter values. Detritus taken from OFAM3 is converted to units of nM Fe from mmol N by using the Redfield ratio of 0.02. As in *Galbraith et al.* [2010], the sinking speed (w_{sink}) is 16 m day^{-1} over the top 80 m, increasing linearly below that depth at a rate of 0.05 (m day^{-1}) m^{-1}.

In order to optimise the scavenging parameterisation, particle pathways are first identified by backtracking particles from 4 EUC sections 165^0E, 170^0W, 140^0W, and 110^0W to the EUC section at 156^0E for our examination of dissolved iron concentrations (and from 4 EUC sections from 156^0E, 165^0E, 170^0W and 140^0W to the EUC section 149^0E for our examination of total dissolved iron concentrations; as observations were available at different locations). See the dashed black line in Figure 1 for the boundaries. Subsequently, we assign observed DFe at 156^0E (149^0E for TDFe) as Fe_{src} to all particles and integrate the iron model forward in time until the Lagrangian particles reach their EUC release sections. Initial source concentrations for off-equatorial interior section boundaries (horizontal black dashed lines in Figure 1d at 2.655°S and 2.655°N) are spatially interpolated between the start (149°E/156°E) and end EUC section iron profiles. We do not calculate iron concentrations backward in time from the EUC because the effect of dilution of different water masses cannot be determined backwards in time.

The comparison between our optimized simulated iron concentrations along the equator and observations is shown in Figure S5. The values are averaged between 0.25^0S–0.25^0N for comparison against the equatorial observations.

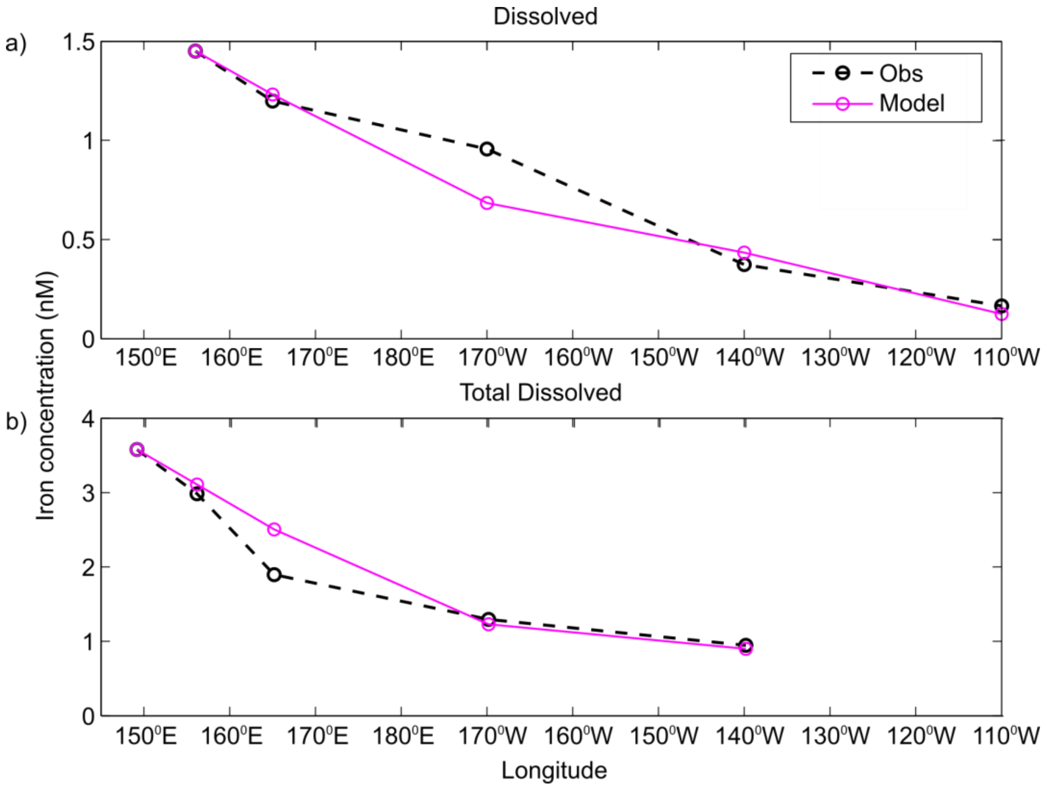

Figure S5. ***Scavenging parameterisation comparison.*** *Fitting the optimal scavenging constants for DFe iron and b) TDFe using the constants specified in the main text and Equation 2 against equatorial iron observations (black dashed).*

Another uncertainty is that the observed profile at 149°E is upstream of a great portion of the NICU waters (see Figure S2 and Figure 2 in *Qin et al*. [2015]). Assuming that additional iron is sourced from the NICU between 149°E and 156°E, using the observed profile at 149°E might result in an underestimate of the scavenging. However, as mentioned previously both the TDFe and DFe concentrations from the off-equatorial boundaries where a possible NICU source is likely to enter were tested with varying concentrations and only resulted in a systematic reduction in iron values.

S6. Backtracking Experiment Setup

Lagrangian particles are released at the core of the EUC along meridional sections ('release' sections) every 6 days. Here, we examine 5 sections at 156^0E, 165^0E, 170^0W, 140^0W, and

110^0W in order to cover the whole EUC from the western basin to the upwelling regions eastwards of 140^0W. The particles are backtracked in the OFAM3 velocity fields until they reach one of eight predefined *source* locations shown in Figure 1: (i) New Guinea Coastal Undercurrent, (ii) New Ireland Coastal Undercurrent, (iii) Mindanao Current, (iv) North Interior, (v) South Interior, (vi) North of EUC, (vii) South of EUC, and (viii) recirculation within the EUC. Note that because particles are assigned to the first section they cross, the NGCU section includes some water that would have eventually intersected with the NICU section. However, this effect turns out to be small, affecting only 2 - 4 % of NICU particles. This definition is to ensure the maximum NGCU transport and thus an upper bound on the iron provided by the NGCU.

S7. Placing bounds on iron processes

In our Lagrangian treatment of iron, there are four processes affecting iron concentration. These are the biological activity (phytoplankton uptake and remineralisation), scavenging and mixing of water masses with differing amounts of iron. While scavenging has been optimised to fit the observed equatorial EUC concentrations, uncertainties may remain in the other terms.

Biology can act to both decrease iron through phytoplankton uptake and increase iron through organic matter remineralisation. The combined effect of these two biological terms results in a Fe increase of 0.03 nM from their source sections in the Western Pacific to the Eastern equatorial Pacific at 110°W. This 0.03 nM represents a 20 % increase in the mean EUC iron concentration in the experiments with the lowest concentrations (*BACK*) and only a 6 % increase in mean iron content for an experiment with relatively higher concentrations of iron, (*NGCU-HIGH*). Thus even though there are substantial biases in the OFAM3 phytoplankton distribution (Text S2), this likely has only a small impact on the simulated iron distribution in the Lagrangian model. This is also supported by previous iron sensitivity studies of the EUC such as [*Gorgues et al.* 2010; *Slemons et al.* 2009] where even at higher iron concentrations (9 nM), biological terms had a relatively minor impact on iron compared to enhanced scavenging.

Uncertainty in the iron concentration for the interior sources away from the LLWBCs may also be a factor in the underestimated iron values for *NGCU-LOW* and *NGCU-HIGH*. The sparse open ocean measurements in the Pacific Ocean make assigning accurate iron concentrations to interior waters problematic. As such, the same averaged profile is used for all interior sources (except recirculation where equatorial EUC profiles are available) for the sensitivity experiments. However this background iron profile may be too low. Based on available observations we expect both DFe and TDFe open-ocean iron concentrations from surface to depth to be well below 1.0 nM even in regions of high dust deposition [*Moore and Braucher*, 2008]. In a modification of the *NGCU-LOW* and *NGCU-HIGH* experiments, this upper bound of 1.0 nM is set to all the interior iron sources at all depths except for recirculation from the EUC, which are imposed with the EUC observations. Even with this large increase in interior concentration, an elevated NGCU concentration on its own is still well below the observed value with 1.0 vs 1.5 nM for DFe and 1.8 vs 2.6 nM for TDFe at 156^{0}E (not shown). Moreover, as interior sources make up an increasing fraction of the EUC to the east, the zonal gradient becomes too weaker with elevated background iron concentrations. Thus uncertainties in the open ocean iron sources are unlikely to explain the underestimated EUC iron concentrations resulting from a sole NGCU source.

With regards to the mixing of water masses or dilution of the higher iron concentrations from the LLWBCs by the lower concentrations in the interior water masses, it has been shown in previous studies of *Grenier et al.* [2011] and *Qin et al.* [2015] that the proportion of water from interior circulation increases going eastward thus reducing the high concentration of iron derived from the LLWBC sources by dilution. The amount of dilution is dependent on the proportion of water masses from each source. In our Lagrangian experiments this dilution is set by the physical circulation in OFAM3 and the results in *Qin et al.* [2015] as well as validation of the NGCU in Text S2 suggest that OFAM3 has a reasonable representation of the contribution of water from each source to the EUC.

The final uncertainty is in the imposed NGCU iron concentration given the sparsity of available observations. Two supplementary experiments are performed in which the NGCU source concentrations are elevated so that equatorial iron concentrations more closely match observations. The NGCU source concentration has to be increased by 2.5 times (from 0.5 – 2.0 nM to 1.3 – 5.0 nM) and 2.2 times (from 8 – 9 nM to 17.6 – 19.8 nM) for DFe and for TDFe, respectively. However the total dissolved iron concentrations would then be larger than the upper limit of iron observations of 15.5 nM along similar continental shelf regions [*Bruland et al.*, 2005]. As such, these levels of iron in the NGCU iron are unlikely.

S8. Iron Observation Sources

The observed open ocean dissolved iron profiles that were used to construct the background iron profile in Figure 1a are shown by the red dots in Figure S6. These are specified to be within 156°E – 110°W, 10°S – 10°N and 500 km away from the coastline. The average of these measurements is used as a typical background concentration in our experiments.

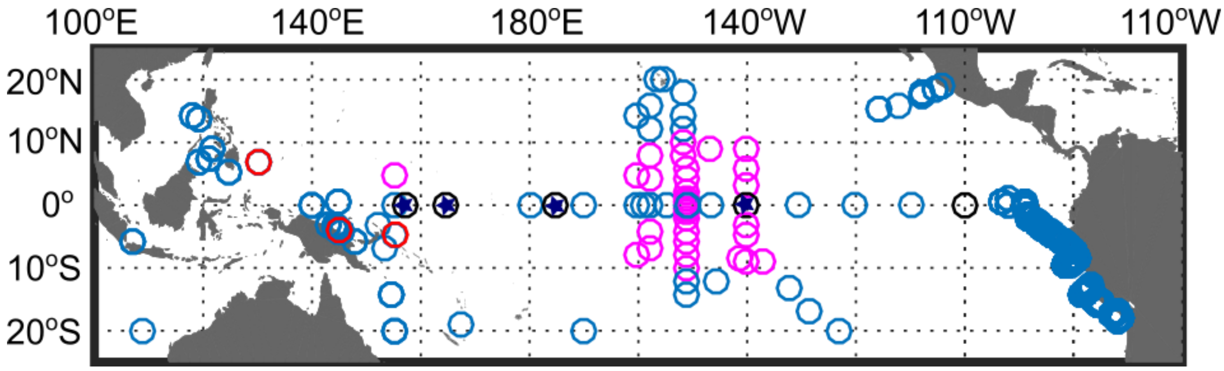

Figure S6. ***Iron measurements.*** *Location of iron measurements made during Tropical Pacific cruises (all symbols). Off-equatorial, DFe measurement away from the coasts used to construct the background iron profile in Figure 1a are shown as magenta circles. Black circles and stars indicate location of equatorial DFe measurements; TDFe measurements are only available at the black stars. These profiles are used for comparison in Figure 1. DFe measurements are from Blain et al, [2008], Coale et al, [1996], DiTullio et al, [1993], Fitzwater et al, [1996], Kaupp et al, [2011], Kondo et al, [2012], Mackey et al, [2002], Slemons et al, [2010], Takeda and Obata, [1995] and Wu et al. [2011]. TDFe observations are taken from Mackey et al, [2002] and Slemons et al, [2010]. Going from east to west, the red data circles indicate locations for the DFe MC source [Kondo et al., 2007], the TDFe and DFe NGCU sources [Slemons et al., 2010] and the DFe NICU source [Slemons et al., 2010].*

Observations of TDFe in the open ocean are very sparse (*Bruland et al.* [1994], *Hansard et al.* [2009], *Jong et al.* [1998], *Martin et al.* [1990] and *Wu and Luther* [1994]) with only the study of *Hansard et al.* [2009] in the Pacific Ocean. These TDFe profiles are shown in Figure S7.

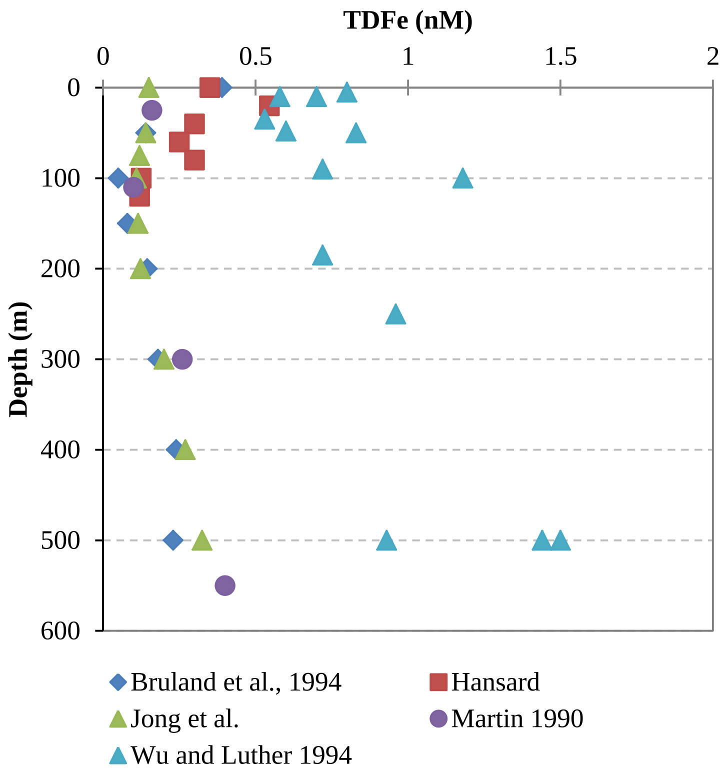

Figure S7. *Vertical profiles of open ocean TDFe measurements.*

Except for the profile from *Wu and Luther* [1994] which is taken from the North Atlantic, the open ocean TDFe measurements are generally below 0.5 nM. For the study of *Wu and Luther* [1994], which displays the highest values, only 3 measurements exceed 1 nM. Given the similarity of the open ocean TDFe profiles to the open ocean DFe profile in Figure 1a (excluding *Wu and Luther* [1994] observations), and the large uncertainties associated with the TDFe profiles, in our experiments we assume that the TDFe follows the DFe background profile. To check the sensitivity of our results to this assumption we perform sensitivity tests described in Text S7 where open ocean concentrations are elevated to 1 nM, (approximately the average of the high *Wu and Luther* [1994] measurements; Figure S7).

S9. Transit time from the western to the eastern Pacific

		156°E	165°E	170°W	140°W	110°W
NGCU	**Max. lagged Correlation**	0.39	0.22	-	-	-
	Lag	180	186	-	-	-
	IQ Range	108 – 339	156 – 356	219 – 488	279 – 642	321 – 763
NGCU&NICU	**Max. lagged Correlation**	0.55	0.46	0.42	0.40	0.41
	Lag	102	162	324	394	410
	IQ Range	18 – 194	51 – 254	123 – 374	189 – 516	210 – 595
Ryan et al. (2006)	**EEP bloom occurs after the maximum NGCU shoaling and intensification**					9-13 months

Table S2. *Maximum lagged correlation between NGCU (2nd row) and NGCI+NICU (5th row) source iron concentration and iron concentration at the various release sections (only correlations significant at 95% level are shown). Also shown are lag associated with the maximum (3rd and 6th rows) and the interquartile particle transit time and the (4th and 7th rows; in days). 8th row: The time difference between the observed NGCUC shoaling and peak intensification compared to equatorial bloom start for three El Niño events from Ryan et al. (2006).*

References

Blain, S., S. Bonnet, and C. Guieu (2008), Dissolved iron distribution in the tropical and subtropical South Eastern Pacific, *Biogeosciences*, *5*(1), 269-280.

Bruland, K. W., Orians, K. J., & Cowen, J. P. (1994). Reactive trace metals in the stratified central North Pacific. Geochimica et Cosmochimica Acta, 58(15), 3171-3182.

Butt, J., and E. Lindstrom (1994), Currents off the east coast of New Ireland, Papua New Guinea, and their relevance to regional undercurrents in the western equatorial Pacific Ocean, *Journal of Geophysical Research: Oceans*, *99*(C6), 12503-12514.

Coale, K. H., S. E. Fitzwater, R. M. Gordon, K. S. Johnson, and R. T. Barber (1996), Control of community growth and export production by upwelled iron in the equatorial Pacific Ocean, *Nature*, *379*(6566), 621-624.

Cravatte, S., A. Ganachaud, Q. P. Duong, W. S. Kessler, G. Eldin, and P. Dutrieux (2011), Observed circulation in the Solomon Sea from SADCP data, *Prog Oceanogr*, *88*(1-4), 116-130.

DiTullio, G. R., D. A. Hutchins, and K. W. Bruland (1993), Interaction of iron and major nutrients controls phytoplankton growth and species composition in the tropical North Pacific Ocean, *Limnology and Oceanography*, *38*(3), 495-508.

De Jong, J. T. M., Den Das, J., Bathmann, U., Stoll, M. H. C., Kattner, G., Nolting, R. F., & De Baar, H. J. W. (1998). Dissolved iron at subnanomolar levels in the Southern Ocean as determined by ship-board analysis. *Analytica Chimica Acta*, *377*(2), 113-124.

Fitzwater, S. E., K. H. Coale, R. M. Gordon, K. S. Johnson, and M. E. Ondrusek (1996), Iron deficiency and phytoplankton growth in the equatorial Pacific, *Deep Sea Research Part II: Topical Studies in Oceanography*, *43*(4), 995-1015.

Galbraith, E. D., A. Gnanadesikan, J. P. Dunne, and M. R. Hiscock (2010), Regional impacts of iron-light colimitation in a global biogeochemical model, *Biogeosciences*, *7*(3), 1043-1064.

Gledhill, M., and K. N. Buck (2012), The organic complexation of iron in the marine environment: a review, *Frontiers in microbiology*, *3*.
Gorgues, T., C. Menkes, L. Slemons, O. Aumont, Y. Dandonneau, M. H. Radenac, S. Alvain, and C. Moulin (2010), Revisiting the La Nina 1998 phytoplankton blooms in the equatorial Pacific, *Deep-Sea Res Pt I*, *57*(4), 567-576.
Grenier, M., S. Cravatte, B. Blanke, C. Menkes, A. Koch-Larrouy, F. Durand, A. Melet, and C. Jeandel (2011), From the western boundary currents to the Pacific Equatorial Undercurrent: Modeled pathways and water mass evolutions, *J Geophys Res-Oceans*, *116*.
Hansard, S. P., Landing, W. M., Measures, C. I., & Voelker, B. M. (2009). Dissolved iron (II) in the Pacific Ocean: Measurements from the PO2 and P16N CLIVAR/CO 2 repeat hydrography expeditions. *Deep Sea Research Part I: Oceanographic Research Papers*, *56*(7), 1117-1129.
Johnson, G., B. M. Sloyan, W. S. Kessler, and K. E. McTaggart (2002), Direct measurements of upper ocean currents and water properties across the tropical Pacific during the 1990s, *Prog Oceanogr*, *52*(1), 31-61.
Kaupp, L. J., C. I. Measures, K. E. Selph, and F. T. Mackenzie (2011), The distribution of dissolved Fe and Al in the upper waters of the Eastern Equatorial Pacific, *Deep Sea Research Part II: Topical Studies in Oceanography*, *58*(3–4), 296-310.
Kondo, Y., S. Takeda, and K. Furuya (2007), Distribution and speciation of dissolved iron in the Sulu Sea and its adjacent waters, *Deep Sea Research Part II: Topical Studies in Oceanography*, *54*(1–2), 60-80.
Mackey, D. J., J. E. O'Sullivan, and R. J. Watson (2002), Iron in the western Pacific: a riverine or hydrothermal source for iron in the Equatorial Undercurrent?, *Deep-Sea Res Pt I*, *49*(5), 877-893.
Martin, J. H., Gordon, R. M., & Fitzwater, S. E. (1990). Iron in Antarctic waters. Nature, 156-158.
Moore, J. K., and O. Braucher (2008), Sedimentary and mineral dust sources of dissolved iron to the world ocean, *Biogeosciences*, *5*(3), 631-656.
Oke, P. R., D. A. Griffin, A. Schiller, R. J. Matear, R. Fiedler, J. Mansbridge, A. Lenton, M. Cahill, M. A. Chamberlain, and K. Ridgway (2012), Evaluation of a near-global eddy-resolving ocean model, *Geosci. Model Dev. Discuss.*, *5*(4), 4305-4354.
Qin, X., A. Sen Gupta, and E. van Sebille (2015), Variability in the origins and pathways of Pacific equatorial undercurrent water, *Journal of Geophysical Research: Oceans*, *120*(4), 3113–3128.
Raiswell, R., and D. E. Canfield (2012), The iron biogeochemical cycle past and present, *Geochemical Perspectives*, *1*(1), 1-2.
Ryan, J. P., I. Ueki, Y. Chao, H. Zhang, P. S. Polito, and F. P. Chavez (2006), Western Pacific modulation of large phytoplankton blooms in the central and eastern equatorial Pacific, *Journal of Geophysical Research: Biogeosciences*, *111*(G2), G02013.
Slemons, L., B. Paul, J. Resing, and J. W. Murray (2012), Particulate iron, aluminum, and manganese in the Pacific equatorial undercurrent and low latitude western boundary current sources, *Mar Chem*, *142*, 54-67.
Slemons, L., T. Gorgues, O. Aumont, C. Menkes, and J. W. Murray (2009), Biogeochemical impact of a model western iron source in the Pacific Equatorial Undercurrent, *Deep-Sea Res Pt I*, *56*(12), 2115-2128.
Slemons, L., J. W. Murray, J. Resing, B. Paul, and P. Dutrieux (2010), Western Pacific coastal sources of iron, manganese, and aluminum to the Equatorial Undercurrent, *Global Biogeochem Cy*, *24*.
Tagliabue, A. (2015), Dissolved Iron Database, edited.

Takeda, S., and H. Obata (1995), Response of equatorial Pacific phytoplankton to subnanomolar Fe enrichment, *Mar Chem*, *50*(1), 219-227.

Ueki, I., Y. Kashino, and Y. Kuroda (2003), Observation of current variations off the New Guinea coast including the 1997–1998 El Niño period and their relationship with Sverdrup transport, *Journal of Geophysical Research: Oceans*, *108*(C7).

Wu, J., and Luther III, G. W. (1994). Size-fractionated iron concentrations in the water column of the western North Atlantic Ocean. *Limnology and Oceanography*, *39*(5), 1119-1129.